

Article www.acsanm.org

Cu₂S@Bi₂S₃ Double-Shelled Hollow Cages as a Nanocatalyst with Substantial Activity in Peroxymonosulfate Activation for Atrazine **Degradation**

Ahmed E. ElMetwally, Farnoosh Goodarzi, Katlyn K. Meier, Elsayed M. Zahran, Sundeep Rayat, Søren Kegnæs, Marc R. Knecht, and Leonidas G. Bachas*



Cite This: ACS Appl. Nano Mater. 2021, 4, 12222-12234



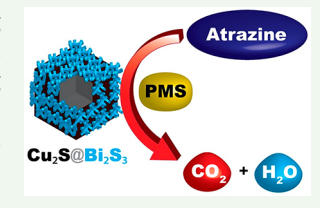
ACCESS

III Metrics & More

Article Recommendations

Supporting Information

ABSTRACT: Metal dichalcogenides are promising candidates for heterogeneous catalysis. Designing them as a double-shelled hollow nanostructure can enhance their performance owing to the high surface area provided by the hollow inner space. Herein, we demonstrate a multistage templating approach to prepare double-shelled cages with Bi₂S₃ nanoparticles as an outer shell and Cu₂S as an inner shell. A facile deposition method, coupled with a benign sulfidation process, has been developed to prepare such a double-shelled hollow structure. The prepared Cu₂S@Bi₂S₃ double-shelled cages demonstrated a substantial catalytic reactivity in peroxymonosulfate (PMS) activation for the degradation of atrazine in the dark. Such performance is attributed to the synergy between Cu₂S and



Bi₂S₃ in activating PMS, which promotes radical generation and enhances the catalytic performance. Our mechanistic studies revealed that hydroxyl radicals and singlet oxygen are the dominant species generated during atrazine degradation.

KEYWORDS: metal dichalcogenides, hollow structure, double-shelled cages, degradation, peroxymonosulfate, atrazine

INTRODUCTION

Peroxymonosulfate (PMS) activation has emerged as a promising process that can generate highly reactive radicals for the degradation of organic contaminants in the absence of any irradiating source. 1,2 PMS possesses an asymmetric structure and a long superoxide O-O bond, which facilitates the activation of the molecule in the presence of a suitable catalyst.3 Several metal oxides have been extensively used for PMS activation as catalysts; 4-6 however, the use these materials has many drawbacks including inefficiency, nonrecyclability, and toxicity.3 Thus, the development of a heterogeneous catalyst that can overcome the drawbacks of metal oxides is highly important. To the best of our knowledge, the use of metal dichalcogenides for PMS activation has not been sufficiently explored, and the mechanism of PMS activation using metal dichalcogenides remains unclear. For example, WS₂ nanosheets were prepared and demonstrated high efficiency for PMS activation for diclofenac degradation. MoS₂ nanoflowers were also shown to be efficient piezocatalysts in PMS activation for phenol degradation. Moreover, 1 T-2H MoS₂ showed a high activation efficacy for PMS during the degradation of butyl paraben.8 Finally, vacancy-rich N@FexOy@MoS2 carbonaceous beads were developed and tested in norfloxacin degradation via PMS activation.9

Metal dichalcogenides are a class of layered materials with a general formula of MX₂, where a layer of metal (M) atoms lies between two layers of chalcogen (X) atoms. The structure of metal dichalcogenides can be classified according to their

atomic arrangement into trigonal prismatic, octahedral, and distorted phases. Layered metal dichalcogenides have a common metal to chalcogen ratio of 1:2; however, there are other types of metal dichalcogenides that have ratios of 2:3 with a formula of M_2X_3 and 1:1 with a formula of MX. 10,11 Earth-abundant transition metal dichalcogenides have attracted much attention for various applications because of their low health and environmental impact, low cost, as well as their stoichiometric, compositional, and structural versatility. Metal dichalcogenides have been employed extensively as catalysts in hydrogen evolution reactions, 12-14 while others have been explored as catalysts for oxygen evolution reactions. 15,16

Among these metal dichalcogenides, copper-based chalcogenides have revealed an outstanding activity in biological and sustainable energy devices because of their intriguing properties.¹⁷ Copper sulfide (Cu_{2-x}S) has an intricate binary structure, which obscures the evaluation and nomenclature of its crystal phase. The properties of different copper sulfide phases are extremely sensitive in terms of the Cu-S crystal structure and stoichiometry, and thus, tuning the crystal phase is necessary to control the target properties. The binary Cu-S system has diverse crystal phases that include various

Received: September 1, 2021 Accepted: October 27, 2021 Published: November 17, 2021





nonstoichiometric compositions, which give rise to eight crystal phases within the system. 18 Among these crystal phases, Cu_2S has been used in different applications including cold cathodes, solar cells, and nanoscale switches. 19,20

When employed as a catalyst, Cu₂S nanoplates showed significant oxygen evolution for water oxidation in the presence of glycine. Furthermore, Cu₂S microcrystals with rod-like morphologies have been shown to be effective in the catalytic degradation of methylene blue in the presence of hydrogen peroxide. Porous 3D hierarchical Cu₂S microsponges were reported as efficient catalysts in phenol degradation under visible light. Cu₂S demonstrated an adequately high yield in the catalytic cross-coupling of aryl iodides with diaryl disulfides. Furthermore, Cu₂S has been interfaced with other semiconductors such as in MoS₂/Cu₂S, Cu₂S-Pd₄S, Cu₂S/Bi₂WO₆, and Cu₂S/Ag₂S/BiVO₄ to enhance the photocatalytic performance of the heterostructure. However, Cu₂S has not yet been explored as a catalyst in PMS activation for the degradation of emerging contaminants.

Bi₂S₃ is a V-VI semiconducting material that has been used frequently in different applications including lithium-ion batteries, gas sensors, Schottky diodes, and X-ray computed tomography imaging. $^{29-32}$ Bi $_2$ S $_3$ commonly forms one-dimensional nanostructures, such as ribbons, tubes, rods, and wires, with an orthorhombic crystal structure. These nanoarchitectures exhibit a 2-D layered structure stacked via van der Waals forces. As a semiconductor, Bi₂S₃ has been used individually and in heterostructures for various photocatalytic applications. For instance, Bi₂S₃ nanorods have been employed as a photocatalyst for rhodamine B degradation with a significant degradation performance.³³ Bi₂S₃ has been introduced as an ntype semiconductor to promote the photocatalytic performance of heterostructures such as Bi₂S₃/Bi₂O₃/Bi₂O₂CO₃, $Bi_2S_3/BiOBr$, Bi_2S_3/Bi_2WO_6 , $Bi_2S_3/BiOCl$, $BiOBr/Bi_2S_3$, and $Bi_2S_3-UiO-66$. However, there is no report published yet regarding the use of Bi₂S₃ nanoparticles as a catalyst for PMS activation.

Hollow nanostructures have attracted much attention, especially in the field of catalysis, because of their architectural properties such as low density, multiple interfaces, large surface-to-volume ratio, and diminished diffusion lengths for mass transfer. Moreover, double-shelled hollow structures enhance the catalytic performance owing to their ability to exploit their inner space and to provide a high surface area. The double-shelled crust enhances the mechanical stability of the hollow materials and, consequently, can boost catalytic performance while maintaining durability.

Herein, we demonstrate a new approach to construct hierarchical Cu₂S@Bi₂S₃ double-shelled cages using Cu₂O cubes as a template. Initially, Cu₂O cubes were prepared and used as a template for the deposition of BiOBr nanosheets. Next, the obtained Cu₂O@BiOBr core-shell cubes were sulfidized using an alkaline Na₂S solution at 0 °C and under a N₂ atmosphere to avoid the oxidation of Cu₂O and to obtain Cu₂O@Cu₂S@Bi₂S₃ core-shell cubes. Lastly, the Cu₂O core was selectively etched to obtain Cu₂S@Bi₂S₃ double-shelled cages. To our knowledge, this is the first study that depicts the construction of such double-shelled cages for catalysis. The prepared materials were characterized using scanning electron microscopy (SEM), transmission electron microscopy (TEM), powder X-ray diffraction (XRD), X-ray photoelectron spectroscopy (XPS), near-infrared spectroscopy, elemental mapping, and textural analysis. Next, their catalytic reactivity was

evaluated in PMS activation for atrazine degradation in the absence of any irradiation. The mechanism of PMS activation was investigated by monitoring the reaction rate in the presence of radical scavengers and by detecting the radicals generated using electron paramagnetic resonance (EPR) analysis. Total organic carbon (TOC) analysis was used to measure the extent of atrazine mineralization. The prepared $\text{Cu}_2\text{S@Bi}_2\text{S}_3$ double-shelled cages demonstrated a substantial catalytic activity in PMS activation for the degradation of atrazine contaminants, showing superior catalytic performance when compared with previously reported catalysts. These findings manifest that the precise design of hierarchical double-shelled cages can be a promising approach to prepare highly efficient materials that can be used as a platform for different applications.

EXPERIMENTAL SECTION

Materials. Copper sulfate pentahydrate, polyvinylpyrrolidone (average MW $\sim 29\,000$), sodium bromide, sodium citrate tribasic dihydrate, atrazine, potassium peroxymonosulfate, 2,2,6,6-tetramethylpiperidine, and sodium carbonate were obtained from Sigma-Aldrich. Sodium sulfide, sodium azide, and bismuth nitrate pentahydrate were obtained from Acros Organics. Ethylene glycol, p-benzoquinone, and tert-butyl alcohol were purchased from Alfa Aesar. Absolute ethanol was purchased from Pharmco Aaper. 5,5-Dimethyl-1-pyrroline-N-oxide was obtained from Enzo Life Sciences. Milli-Q water was used throughout the study.

Preparation of Cu₂O@BiOBr Core-Shell Cubes. Cu₂O cubes were prepared using a procedure described in our previous Selected amounts of the obtained Cu₂O cubes were ultrasonically dispersed in 100 mL of an ethylene glycol-H₂O (90:10 v/v) solution containing 0.32 g of BiNO₃·5H₂O. Two different loadings of BiOBr with bismuth contents of 22 and 44 wt % were prepared by controlling the amount of the Cu₂O template. The resultant slurry was stirred overnight at room temperature. Next, 10 mL of ethylene glycol containing 0.07 g of NaBr was added to the slurry at room temperature. Lastly, the mixture was transferred to a 250 mL round-bottom flask that was then immersed in an oil bath at 120 °C for 5 h. The obtained solids were filtered, washed, and dried overnight in vacuo at 60 °C. The two different loadings of the coreshell cubes are denoted as Cu₂O@BiOBr (22 wt %) and Cu₂O@ BiOBr (44 wt %) where the wt % represents the bismuth content in the sample.

Preparation of Cu₂O@Cu₂S@Bi₂S₃ Core—Shell Cubes. The obtained Cu₂O@BiOBr core—shell cubes were ultrasonically dispersed in 50 mL of deionized water, and the mixture was then transferred to a double-jacketed reactor. The suspension was purged with ultrapure nitrogen for 30 min, and the reactor temperature was adjusted to 0 °C. Next, a mixture of Na₂S (0.01 M) and NaOH (0.001 M) was added dropwise to the suspension under stirring. The mixture was stirred under a nitrogen atmosphere for 20 min at 0 °C. The obtained solids were filtered, washed, and dried overnight *in vacuo* at 60 °C.

Preparation of $Cu_2S@Bi_2S_3$ Double-Shelled Cages. The obtained $Cu_2O@Cu_2S@Bi_2S_3$ core—shell cubes were soaked in an ammonia solution (12%) for 72 h to dissolve the Cu_2O core. The obtained $Cu_2S@Bi_2S_3$ double-shelled cages were filtered, washed, and dried overnight *in vacuo* at 60 °C. The two different loadings of the double-shelled cages are denoted as $Cu_2S@Bi_2S_3$ (22 wt %) and $Cu_2S@Bi_2S_3$ (44 wt %) where the wt % represents the bismuth content in the sample. Cu_2S hollow cubes were also prepared for comparison using Cu_2O cubes as a template.

Characterization. SEM images of the prepared materials were obtained using a FEI XL-30 Field Emission ESEM/SEM operating at 20 kV. To prepare the samples, 5 mg was dispersed in 200 μ L of absolute ethanol using a sonicator, from which 50 μ L of the dispersed material was drop-casted onto an aluminum stub. Energy-dispersive X-ray spectroscopy (EDS) was performed using SEM-EDS elemental

mapping by studying the sample with an electron scanning microscope (Quanta 200 ESEM FEG) operated at 20 keV and equipped with an Oxford Instruments X-Max 50 mm² EDS analyzer using Aztec 3.3 Service Pack 1 software for data analysis. The samples were prepared according to the aforementioned procedure for SEM sample preparation. An Agilent 720 ICP-OES spectrometer was used to quantify the concentration of the elements in the samples.

TEM images were obtained on a JEOL JEM-1400 microscope operating at 80 kV. To prepare the TEM samples, the materials (5 mg) were ultrasonically dispersed in absolute ethanol (200 μ L), from which 5 μ L of the dispersed solids was drop-casted onto a carboncoated 200 mesh Cu grid. HRTEM was conducted on a FEI F200i S/ TEM operating at 200 kV with a X-twin objective lens pole piece; the instrument is equipped with a FEI Ceta 16-megapixel camera, a Fischione Instruments Model 3000 STEM detector, and a Bruker XFlash 6T|30 windowless silicon drift detector (30 mm² detector area) for EDS and line scan profile analyses. The HRTEM sample was prepared according to the procedure discussed previously, but the sample was drop-casted on a Au grid instead of Cu grid for elemental mapping.

XRD diffraction patterns were obtained on a Philips model PW 3710 instrument using Cu K α radiation. XPS analysis was conducted using a PHI 5000 Versa Probe II equipped with a focused monochromatic Al K α source. Near infrared spectra of the prepared samples were obtained on a Cary 5000 UV-vis-NIR spectrophotometer. The materials were ultrasonically dispersed in ethanol and then placed in a quartz cuvette with a 1.0 cm path length. Nitrogen physisorption was performed at liquid nitrogen temperature on a Micromeritics 3Flex surface area and porosimetry analyzer. Prior to the measurement, samples were outgassed under a vacuum at 50 °C overnight. The specific surface area (S_{BET}) was calculated from the N_2 adsorption data by the BET method in the relative range (P/P_0) of 0.05–0.3. Finally, the total pore volume $(V_{\rm total})$ was calculated from the amount of adsorbed nitrogen at a relative pressure of $P/P_0 = 0.95$.

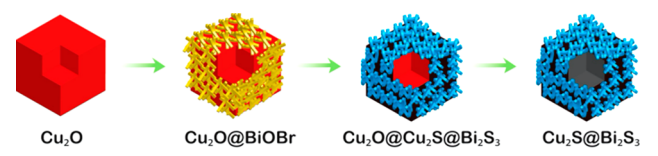
Catalytic Activation of Peroxymonosulfate (PMS) for Atrazine Degradation. For each catalytic experiment, a 60 mL aluminum foil-wrapped vial was filled with 50 mL of atrazine solution (4.6 μ M), to which 10 mg of the prepared catalyst was ultrasonically dispersed for 10 s in a Branson M2800 ultrasonic bath. The reaction mixture was stirred for 30 min to attain adsorption-desorption equilibrium. To initiate the catalytic reaction, 1 mM PMS was added, and the reaction mixture was stirred for 2 h. At specific time intervals, aliquots (900 µL) were withdrawn and mixed with 500 µL of methanol to quench the reaction. Next, the quenched samples were centrifuged to separate the solid catalyst. Afterward, 500 µL of the supernatant was transferred to a vial and analyzed using HPLC. A Dionex UltiMate 300 HPLC equipped with a UV-vis diode array detector adjusted to 222 nm was used during the analysis. The analysis was conducted using a mobile phase ($H_2O/CH_3CN = 1:1$) with a flow rate that was set at 1 mL min⁻¹ on an Agilent Eclipse Plus C18 column (3.5 μ m × 4.6 mm × 100 mm). Electron paramagnetic resonance (EPR) spectra of hydroxyl radicals were collected on a Bruker EMXplus X-band CW EPR spectrometer equipped with a 9.5 in. double yoke magnet. All spectra were recorded at room temperature and at X-band (9.65 GHz) frequency, using a PremiumX ultra low noise microwave bridge and high sensitivity resonator. An ER4116DM dual mode bimodal cavity was also used in this study. EPR data were analyzed and simulated using the SpinCount software package provided by Dr. Michael P. Hendrich of Carnegie Mellon University. 47 EPR spectra of singlet oxygen were collected on a Bruker A300 spectrometer, and data were analyzed and simulated using the WinSim package. TOC analysis was conducted on a Shimadzu TOC-L analyzer.

RESULTS AND DISCUSSION

Materials Characterization. Cu₂O cubes were prepared through the reduction of a copper-citrate complex using glucose as the reducing agent. The cubes were used as a

sacrificial template for the formation of the double-shelled cages as shown in Scheme 1.

Scheme 1. Illustration of the Preparation Strategy of Cu₂S@ Bi₂S₃ Using a Sacrificial Cu₂O Template



The SEM image of the prepared Cu₂O sample (Figure 1a) shows that the obtained material has a uniform cubic structure

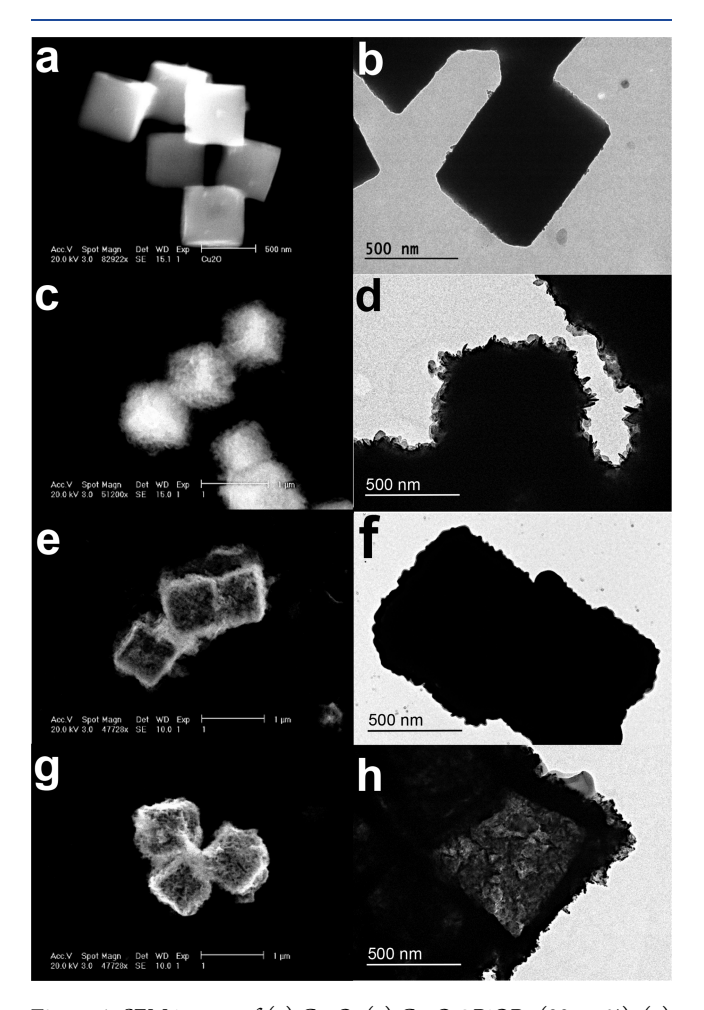


Figure 1. SEM images of (a) Cu₂O₂ (c) Cu₂O@BiOBr (22 wt %), (e) Cu₂O@Cu₂S@Bi₂S₃ (22 wt %), and (g) Cu₂S@Bi₂S₃ (22 wt %) and TEM images of (b) Cu₂O, (d) Cu₂O@BiOBr (22 wt %), (f) Cu₂O@ Cu₂S@Bi₂S₃ (22 wt %), and (h) Cu₂S@Bi₂S₃ (22 wt %).

with a smooth surface. The TEM image of the same sample (Figure 1b) shows that the inner core of the cube is solid. When BiOBr was prepared in the presence of the Cu₂O cubes dispersed in the reaction medium, the BiOBr sheets were formed on the surface of the cubes. Specifically, and to ensure that BiOBr sheets are formed as an outer shell that encapsulates the Cu₂O cube, the cubes were dispersed in a bismuth ion solution and stirred overnight. During this period, the Bi ions were adsorbed onto the surface of the Cu₂O cubes, and consequently, when the BiOBr sheets were formed, they

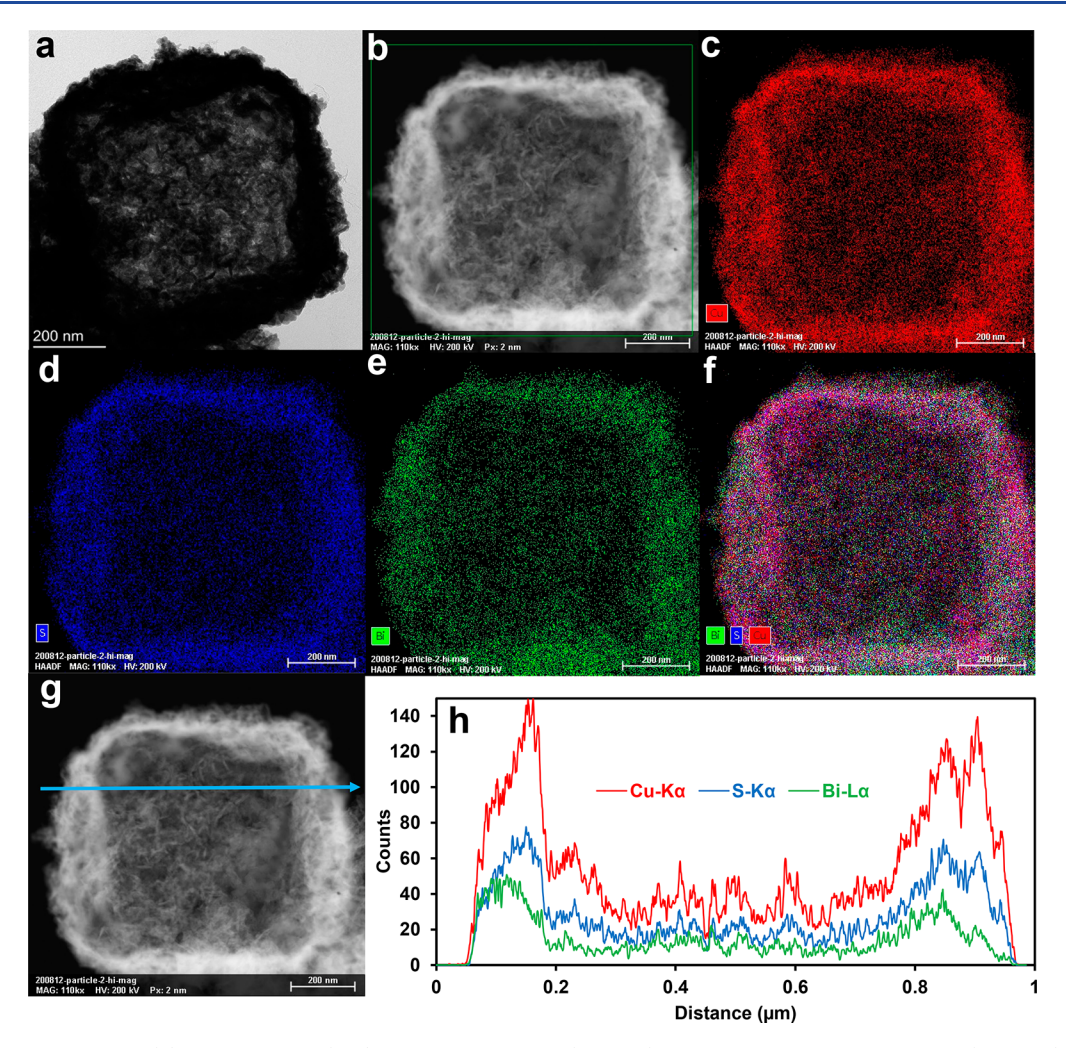


Figure 2. (a) HRTEM image, (b) STEM image, (c-f) EDS mapping, and (g and h) line-scan profile of $Cu_2S@Bi_2S_3$ (22 wt %) double-shelled cage.

were grown on the cube surface. The SEM image of $\text{Cu}_2\text{O}@$ BiOBr (22 wt %) (Figure 1c) reveals that the materials maintain their cubic morphology with an extremely rough surface owing to the deposition of BiOBr. The TEM image of $\text{Cu}_2\text{O}@\text{BiOBr}$ (Figure 1d) demonstrates that the inner core of the cubes remained solid with protruding nanosheets that uniformly cover the Cu_2O .

To investigate the homogeneous distribution of the elements across the prepared Cu₂O@BiOBr core—shell structure, elemental mapping analysis was conducted, and the obtained images are presented in Figure S1a—f. The elemental mapping shows that BiOBr is homogeneously distributed over the surface of the Cu₂O cube to form a shell that encapsulates the inner material. The EDS spectrum of Cu₂O@BiOBr (22 wt %) (Figure S1) displays peaks correspond to the K α X-ray line of copper, bismuth, oxygen, and bromine with a bismuth content of 21.2 \pm 0.5 wt %. To validate these results, the bismuth content was estimated using inductively coupled plasma optical emission spectrometry (ICP–OES); the results revealed that the bismuth content was 22.2 \pm 0.5 wt %, which agrees well with the theoretical calculation for Bi loading of 22 wt %.

The deposition of BiOBr nanosheets over the Cu₂O cubes can be ascribed to the adsorption of bismuth ions on the surface of Cu₂O cubes during the preparation of BiOBr. To

support this explanation, BiOBr was grown on Cu_2O cubes without a preadsorption of bismuth ions, where the NaBr solution was added immediately to the Cu_2O -bismuth ions mixture, and the reaction mixture was then immersed in an oil bath at 120 °C for 5 h. The SEM and TEM images of $Cu_2O@$ BiOBr prepared without bismuth ion preadsorption are shown in the Supporting Information, Figure S2. The images reveal that the BiOBr nanosheets were grown independently from the cubes, with some of the Cu_2O completely uncovered. Thus, the adsorption step is essential to obtaining a uniform $Cu_2O@$ BiOBr core—shell structure.

A higher loading of Cu₂O@BiOBr (44 wt %) was also prepared, and the SEM and TEM images are shown in the Supporting Information, Figure S3. The images reveal that the BiOBr nanosheets form aggregates around the cubes. These aggregates might fuse to form a bulky structure, where the Cu₂O cubic structure became difficult to observe. Moreover, such a nonuniform distribution of BiOBr can significantly affect the catalytic performance of the prepared material; thus, additional analyses were preferentially performed using the Cu₂O@BiOBr (22 wt %) system.

The sulfidation of $Cu_2O@BiOBr$ (22 wt %) was conducted using an alkaline Na_2S solution at 0 °C to form $Cu_2O@Cu_2S@Bi_2S_3$. The SEM image of $Cu_2O@Cu_2S@Bi_2S_3$ (Figure 1e) shows a difference in the texture of the core—shell cubes that

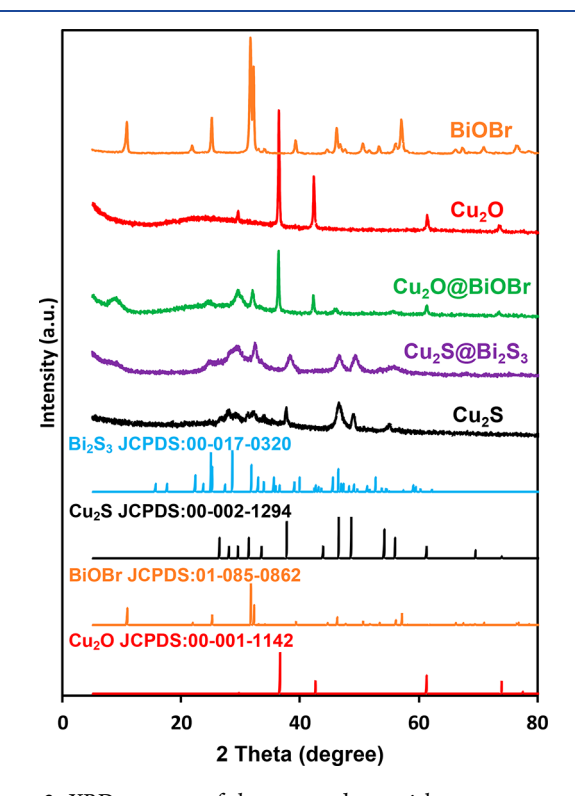
can be ascribed to the transformation of BiOBr nanosheets to Bi₂S₃ nanosheets, which have an entirely different morphology. The TEM image of Cu₂O@Cu₂S@Bi₂S₃ (Figure 1f) shows that the inner core of the cubes remains solid with an outer layer that is vastly different from the flaky texture of Cu₂O@ BiOBr. The SEM and TEM images of Cu₂O@Cu₂S@Bi₂S₃ (44 wt %) (Supporting Information, Figure S3) reveal the alteration of the outer shell morphology upon sulfidation, which is consistent with the images corresponding to the 22 wt % loading. The Cu₂O core was selectively removed by soaking the Cu₂O@Cu₂S@Bi₂S₃ core-shell in ammonia to obtain Cu₂S@Bi₂S₃ double-shelled cages. The SEM image (Figure 1g) reveals the persistence of the cubic structure even after a removal of Cu₂O core. There is no noticeable change in the outer texture of the Cu₂S@Bi₂S₃ double-shelled cages when compared to the Cu₂O@Cu₂S@Bi₂S₃ core-shell; however, the system was noted to be hollow, as anticipated. The TEM image of the Cu₂S@Bi₂S₃ double-shelled cages (Figure 1h) displays a cavity in each cube with an intact outer frame, which presents evidence for the successful removal of the Cu₂O core. The TEM image of the Cu₂S@Bi₂S₃ double-shelled cages (Figure 1h) is consistent with the inner shell composed of Cu₂S particles, while the outer shell is Bi₂S₃ nanosheets. The SEM and TEM images of (44 wt %) loading (Supporting Information, Figure S3) also show the same trend with cavities that are barely visible due to the high loading of Bi₂S₃ nanosheets. The HRTEM and STEM images of Cu₂S@Bi₂S₃ (Figure 2a,b) affirm the hierarchical hollow structure of the prepared double-shelled cages as they show a void in the core of the double-shelled cage, which also confirms the successful removal of the Cu₂O inner core.

The elemental mapping analysis of the Cu₂S@Bi₂S₃ (Figure 2) reveals that the intensities corresponding to copper, bismuth, and sulfur elements are higher at the edge of the double-shelled cage than at the middle, asserting the hollowness of the double-shelled cage. It is evident that the intensity of copper decreased after the removal of the Cu₂O inner core, which indicates that the remaining Cu₂S forms a subtle inner shell that is wrapped with a Bi₂S₃ outer shell. Moreover, it is clear that the intensity corresponding to the bismuth element is higher at the edges of the cube, indicating that Bi₂S₃ forms the outermost shell of the double-shelled cages. On the contrary, the intensities of all elements are extremely low at the center of the cube, consistent with the presence of a void within the double-shelled cages. Interestingly, the line-scan profile of Cu₂S@Bi₂S₃ (Figure 2g,h) exhibits a U-shaped decline, validating the data obtained from elemental mapping, where the intensities of all the elements at the edges are higher than the center. Furthermore, the EDS spectrum (Figure S4) displays the $K\alpha$ X-ray line of copper, bismuth, and sulfur; however, the bismuth content increased to 44.6 \pm 0.5 wt %. This can be ascribed to the removal of the Cu₂O core, which reduced the copper content in the sample. This result was also validated by ICP-OES analysis, where the bismuth content was estimated to be 45.8 \pm 0.5 wt %.

Cu₂S hollow cubes were also prepared for comparison using Cu₂O cubes as a template as shown in Scheme S1. When Cu₂O cubes are sulfidized using Na₂S, a Cu₂O@Cu₂S coreshell structure is formed (Figure S5) owing to the low solubility of Cu₂S in Na₂S solution, and thus, Cu₂O cubes are instantly transformed to a Cu₂O@Cu₂S core—shell. This phenomenon can be attributed to the Kirkendall effect, where

the diffusion of sulfur atoms is much faster than that of oxygen atoms in the cuprous oxide lattice. To remove the inner Cu_2O core, the Cu_2O @ Cu_2S core—shell cubes were soaked in ammonia solution for 72 h to obtain Cu_2S hollow cubes, as shown in Figure S5. It is clear that the Cu_2S hollow cubes inherit the hierarchical cubic framework of the Cu_2O template. The homogeneity of copper and sulfur elements across the Cu_2S hollow cubes was investigated by elemental mapping, and the obtained images are presented in Figure S6a—d. The images reveal that the two elements are uniformly distributed across the hollow cube and particularly at the edges to form a crust that constitutes the cornerstone of the hollow cube. The EDS spectrum of Cu_2S (Figure S6e) displays the peaks that correspond to the $K\alpha$ X-ray line of copper and sulfur with a ratio of 2:1.

To validate the structure of the prepared materials, XRD analysis was conducted for all the samples (Figure 3). The



 $\textbf{Figure 3.} \ \, \textbf{XRD} \ \, \textbf{patterns of the prepared materials}.$

XRD pattern of the Cu_2O cubes exhibits peaks at $2\theta = 29.6^{\circ}$, 36.5°, 42.4°, 61.6°, and 73.9°, which are ascribed to Cu₂O reflection planes, consistent with previous reports. 44 Bare BiOBr was also prepared and characterized using XRD analysis, and the obtained pattern is displayed in Figure 3. The pattern exhibits peaks at $2\theta = 10.8^{\circ}$, 22.1° , 25.2° , 31.6° , 32.2° 46.4° , 56.2° , and 57.2° corresponding to the reflection planes of BiOBr. 49 The pattern of the Cu₂O@ BiOBr core-shell shows the characteristic peaks of both Cu₂O and BiOBr, which indicates that the Cu₂O cubes were able to sustain the preparation conditions of BiOBr without altering its crystal structure. The XRD pattern of the Cu₂S cube (control sample) exhibits a typical diffraction pattern that can be indexed to orthorhombic Cu₂S (JCPDS No. 00-002-1294).⁵⁰ Finally, the XRD pattern of Cu₂S@Bi₂S₃ double-shelled cages displays the characteristic peaks of both Cu₂S and Bi₂S₃. The pattern of Bi_2S_3 can be indexed to the orthorhombic phase of Bi_3S_3 (JCPDS No. 00-017-0320).⁵¹

To elucidate the elemental composition of Cu₂S@Bi₂S₃ double-shelled cages, XPS analysis was conducted, and the obtained spectra are displayed in Figure 4. The XPS spectrum

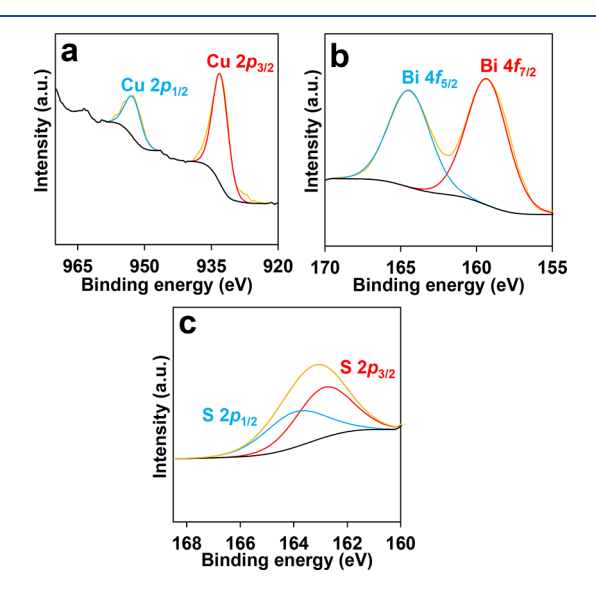


Figure 4. (a) XPS narrow band spectrum of Cu 2p, (b) XPS narrow band spectrum of Bi 4f, and (c) XPS narrow band spectrum of S 2p.

of Cu 2p (Figure 4a) shows two peaks at 932.4 and 952.4 eV that correspond to the binding energies of Cu $2p_{3/2}$ and Cu $2p_{1/2}$, respectively; these values can be indexed to Cu^{+} in $Cu_2S.^{23,45,52,53}$ The Bi 4f spectrum (Figure 4b) shows two major peaks at 159 and 164 eV, which are ascribed to the spin states of Bi $4f_{7/2}$ and Bi $4f_{5/2}$ in $Bi_2S_3.^{34,54}$ The XPS spectrum of S 2p (Figure 4c) shows two peaks at 162.5 and 163.6 eV that correspond to S $2p_{3/2}$ and S $2p_{1/2}$, respectively. 53 Taken together, the XPS results are fully consistent with a sample composed of both Cu_2S and Bi_2S_3 .

To characterize the optical properties of the prepared $\text{Cu}_2\text{S@Bi}_2\text{S}_3$ double-shelled cages, NIR analysis was conducted. The obtained spectrum is displayed in the Supporting Information, Figure S7. It is well-known that CuS materials have a strong plasmon band at 1300 nm in NIR. In contrast to CuS, Cu₂S lacks free charge carriers and thus does not exhibit localized surface plasmon resonance. Fully consistent with this, the present $\text{Cu}_2\text{S@Bi}_2\text{S}_3$ materials displayed no plasmonic properties in the near-IR.

To quantify the surface area of the prepared materials, N2 physisorption analysis was conducted, and the obtained isotherms are presented in Figure S8. All the samples exhibit reversible type II isotherms that are encountered when physisorption occurs on nonporous or macroporous material as a result of unrestrained monolayer-multilayer adsorption. The nonporosity of the tested samples is confirmed by the BJH curves of the desorption branch (Supporting Information, Figure S9), where no defined peak with a defined range is observed. These data agree well with SEM analysis, where the images show that the particles exhibit nonporous texture. The surface area calculated using the BET method, and the total pore volumes obtained from single point adsorption at P/P_0 = 0.95 for all samples are listed in Table 1. The data show that the surface area of the Cu₂O cubes decreased upon BiOBr deposition. On the contrary, when Cu₂O and Cu₂O@BiOBr

Table 1. Textural Properties of the Prepared Samples

sample	$S_{\rm BET}~(\rm m^2 g^{-1})$	$V_{\rm total}~({ m cm}^3~{ m g}^{-1})$
Cu_2O	5.52	0.0067
Cu ₂ O@BiOBr	3.32	0.0047
Cu ₂ S	11.18	0.0285
$Cu_2S@Bi_2S_3$	6.93	0.0117

were sulfidized and the Cu_2O core was eliminated, their surface area roughly doubled (referred to as S_{BET} of Cu_2S and $Cu_2S@$ Bi_2S_3 , respectively). Such an increase can be attributed to the hollow structure of both materials. Moreover, the total pore volume of Cu_2S is higher than that of Cu_2O by 4-fold, while the total pore volume of $Cu_2S@Bi_2S_3$ is higher than that of $Cu_2O@BiOBr$ by 2.5-fold, which also is consistent with the hollow morphology.

Catalytic Activity. The catalytic performance of the $Cu_2S@Bi_2S_3$ double-shelled cages was explored in the degradation of atrazine *via* the activation of PMS. For such experiments, a 4.6 μ M atrazine solution was used throughout the study in the presence of potassium peroxymonosulfate as a radical generating oxidant. All reactions were conducted in the dark at room temperature, unless mentioned otherwise.

It is well-known that hollow nanostructured materials tend to have higher surface areas than their solid counterparts. For this, we carried out experiments to estimate the adsorption capacity of the prepared hollow nanostructured materials, where the obtained data are presented in the Supporting Information, Figure S10. The atrazine adsorption capacity of Cu₂S was compared to those of Cu₂S@Bi₂S₃ (22 wt %) and Cu₂S@Bi₂S₃ (44 wt %). Figure S10 shows that 30 min of stirring in the dark was sufficient to attain adsorptiondesorption equilibrium. The Cu₂S hollow cubes and the Cu₂S@Bi₂S₃ double-shelled cages displayed almost the same adsorption capacity (2.3%) after 3 h, suggesting that the slight difference in surface areas has an insignificant effect on the adsorption capacity of the tested materials. A control experiment was conducted using potassium peroxymonosulfate in absence of any catalyst, and the degradation extent of atrazine was monitored over time. Figure 5 presents an insignificant degradation of atrazine (4.5%) in the absence of catalyst after 3 h of the reaction. Consequently, the presence of the Cu₂S@Bi₂S₃ double-shelled cages in the reaction is required to activate the radical mechanism of PMS.

To evaluate the catalytic performance of the prepared hollow nanostructured materials, 10 mg of each sample was ultrasonically dispersed in 50 mL of atrazine solution (4.6 μ M) and kept under stirring for 30 min to attain adsorptiondesorption equilibrium. The reaction was initiated by adding a certain amount of potassium peroxymonosulfate, and the degradation extent was monitored over time (Figure 5). The data reveal that the catalytic performance of the studied materials was the highest for $Cu_2S@Bi_2S_3$ (22 wt %) (k = 0.1 min^{-1}); however, the Cu_2S with no Bi_2S_3 was more reactive (k = 0.03 min⁻¹) than the $Cu_2S@Bi_2S_3$ (44 wt %) sample (k = 0.02 min⁻¹). Complete degradation was achieved after 40, 80, and 100 min for Cu₂S@Bi₂S₃ (22 wt %), Cu₂S, and Cu₂S@ Bi₂S₃ (44 wt %), respectively; however, Bi₂S₃ nanoparticles alone were uncapable of completely degrading atrazine even after 120 min.

From the catalytic results of $Cu_2S@Bi_2S_3$ (22 wt %), it can be inferred that the incorporation of the Bi_2S_3 outer shell markedly enhanced the catalytic performance. Such enhance-

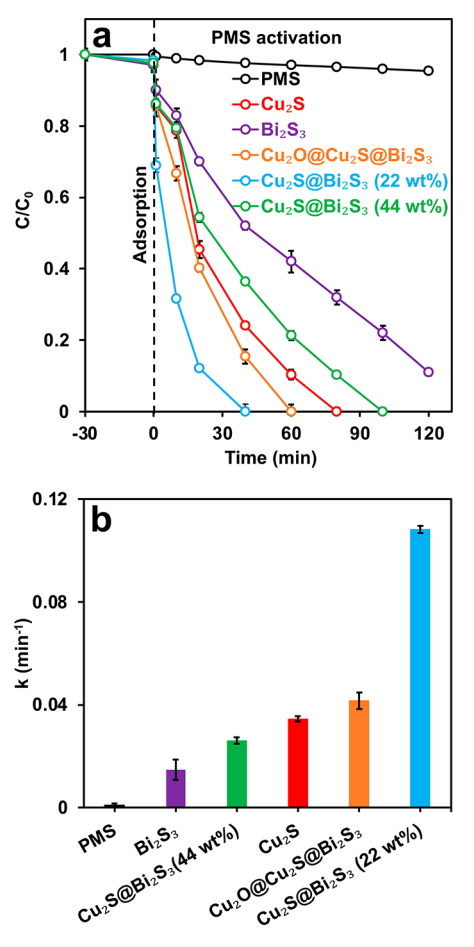


Figure 5. (a) Catalytic degradation and (b) pseudo-first-order rate constants of atrazine (4.6 μ M) using different catalysts (10 mg) and PMS (1 mM) in a total volume of 50 mL.

ment can be attributed to the synergy between Cu₂S and Bi₂S₃ in activating PMS, which promotes radical generation. Moreover, the double-shelled hollow structures can boost the catalytic performance owing to their ability to exploit their inner space and to provide more active sites. 41-43 On the contrary, the reduction of catalytic performance upon the

deposition of a high loading of Bi₂S₃ can be attributed to the aggregation of the catalyst particles. This is consistent with the SEM and TEM images (Supporting Information, Figure S3). The aggregated particles block the active sites and reduce the rate of radical generation. To further evaluate the feasibility of the hollow structure, the catalytic performance of the hollow Cu₂S@Bi₂S₃ was compared with that of the solid Cu₂O@ Cu₂S@Bi₂S₃ cubes, as presented in Figure 5. The data show that the hollow Cu₂S@Bi₂S₃ double-shelled cages exhibit better catalytic activity than their solid counterparts, which highlights the significance of the hollow structure in enhancing the catalytic performance.

It is worth noting that Cu₂S@Bi₂S₃ (22 wt %) showed superior catalytic performance ($k = 0.1 \text{ min}^{-1}$) when compared with previously reported catalysts in atrazine degradation. Li et al. 57 explored the use of Fe₃O₄ in PMS activation for atrazine degradation and found that the tested system was able to degrade atrazine with a rate constant of 0.004 min⁻¹. Chan et also tested the efficacy of CoO/PMS system in atrazine degradation and reported a rate constant of 0.002 min⁻¹. Wang et al. 59 developed a nanoscale perovskite LaFe_{1-x}Cu_xO_{3- δ} and tested its performance in PMS activation for atrazine degradation. They found that the nanoscale perovskite was able to degrade atrazine with a rate constant of 0.04 min⁻¹. Zhang et al.⁶⁰ used a LaCoO₃/Al₂O₃/PMS system to degrade atrazine with a rate constant of 0.017 min⁻¹. The rate constants of other catalysts that were used in PMS activation for atrazine degradation are listed in Table S1. A likely explanation for the enhanced catalytic performance is the synergy between Cu₂S and Bi₂S₃ through a reversible redox reaction. Moreover, metal sulfides are reported to be promising catalysts because of their superior electrical conductivity and low electronegativity over their metal oxide counterparts.⁶¹

The reactivity of Cu₂S@Bi₂S₃ double-shelled cages in atrazine degradation was further examined using naturally sourced tap and lake water. For this comparison, water samples were collected from tap water and lake Osceola, both on the University of Miami campus, and the obtained samples were used as collected without further treatment. Particularly, all the reaction conditions were kept the same as mentioned previously; however, the collected waters were used instead of deionized water to prepare the atrazine stock solution. The

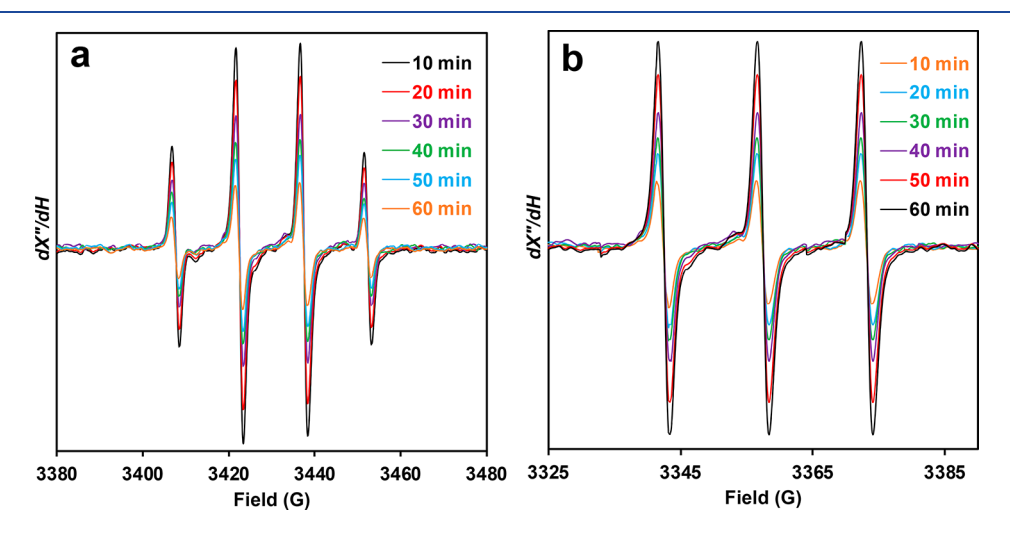


Figure 6. X-band EPR spectra of (a) DMPO-OH adduct and (b) TEMP-1O2 adduct collected under nonsaturating conditions in the presence of Cu₂S@Bi₂S₃ (22 wt %). Experimental conditions: 9.63 GHz frequency, 2.0 mW microwave power, 0.1 mT modulation, and temperature = 20 °C.

obtained data revealed that the degradation of atrazine (Figure S11) in tap water ($k_{\rm obs} = 0.078~{\rm min}^{-1}$) was faster than in lake water ($k_{\rm obs} = 0.03~{\rm min}^{-1}$). Interestingly, the rate constant obtained for the tap water sample was only slightly lower than the rate constant for the reaction conducted in deionized water (0.108 min⁻¹). Despite the reduction in the activity of Cu₂S@ Bi₂S₃ double-shelled cages upon using different waters, the system is still able to degrade the tested model contaminant to a substantial level, which suggests that the developed system is quite efficient at remediating the emerging organic contaminants in different water sources.

To measure the extent of atrazine mineralization, TOC analysis was carried out before and after the reaction. The data showed that almost 95% of atrazine was mineralized after 40 min using $\mathrm{Cu_2S@Bi_2S_3}$ (22 wt %) as a catalyst. Such results demonstrated the efficacy of the prepared double-shelled cages in the degradation of hazardous contaminants that could end up in industrial wastewater effluents. The leaching of metal ions from the double-shelled cages was also examined by monitoring the soluble species after the reaction, all of which were found to be below the limits of detection. Such results suggest that the leached metal ions are not the catalyst in the present system and that the materials do not sufficiently degrade to lead to further environmental contamination.

To understand the mechanism of radical generation, EPR analysis was conducted using 5,5-dimethyl-1-pyrroline N-oxide (DMPO) as a spin trapping reagent. For these studies, 1.6 g L⁻¹ of each catalyst was dispersed in a 2 mL DMPO (0.1 M) solution to which PMS (2 mM) was then added, and the mixture was transferred to a 50 μ L capillary tube for EPR measurements. EPR spectra were collected in 10 min intervals to monitor the radicals generated during PMS activation in the presence of Cu₂S@Bi₂S₃ (22 wt %) as a catalyst. The EPR spectra of Cu₂S@Bi₂S₃ (22 wt %) (Figure 6a) were fit using hyperfine coupling constants of $a_N = 15.12$ G and $a_H = 14.58$ G that correspond to the DMPO adduct of hydroxyl radicals. The simulated and experimental spectra are presented in Figure S12. These values are consistent with the hyperfine coupling constants published elsewhere. 62 The data indicate that hydroxyl radicals are the dominant species generated during the course of the reaction. We monitored the radical generation over the course of 60 min, where it is evident that the EPR signal intensity decreases with time. This effect can be attributed to the consumption of PMS over the course of the reaction. It should be noted that, when the spectrum was collected in the absence of a catalyst, the intensity of the signal was extremely low compared to those of Cu2S and Cu2S@ Bi₂S₃ (22 wt %), as presented in the Supporting Information, Figure S13. In absence of a catalyst, the degradation extent reached 4.5% (referred to as PMS in Figure 5), and according to the EPR data, hydroxyl radicals were the dominant radicals responsible for the degradation of atrazine in the absence of a catalyst. This sluggish level of reactivity in the absence of catalyst arises from the production of an extremely low concentration of hydroxyl radicals. Moreover, the intensity of the signal collected after 10 min for Cu₂S@Bi₂S₃ (22 wt %) is higher than that of Cu2S, confirming that the number of hydroxyl radicals generated when using Cu₂S@Bi₂S₃ (22 wt %) is measurably higher than those produced with Cu₂S. Thus, it can be inferred that the degradation of atrazine is exclusively driven by hydroxyl radicals generated upon the activation of PMS using Cu_2S or $Cu_2S@Bi_2S_3$ (22 wt %).

Additional EPR experiments were conducted to detect the generation of nonradical reactive species using 2,2,6,6tetramethylpiperidine (TEMP) as a spin trapping reagent. For these experiments, 1.6 g L⁻¹ Cu₂S@Bi₂S₃ (22 wt %) was dispersed in a 2 mL TEMP (0.1 M) solution to which PMS (2 mM) was added, and the mixture was transferred to a 50 μ L capillary tube for EPR measurements. EPR spectra were collected in 10 min intervals to monitor nonradical reactive species generated during PMS activation. The EPR spectra (Figure 6b) were fit using a hyperfine coupling constant of a_N = 17.13 G that corresponds to the TEMP adduct of singlet oxygen (1O2). The simulated and experimental spectra are presented in Figure S14. We also monitored the singlet oxygen generation over the course of 60 min, where it is evident that the signal intensity increases with time, which can be attributed to the accumulation of singlet oxygen molecules over the course of the reaction. It is worth noting that there was no signal observed when the spectrum was collected in the absence of a catalyst, as presented in the Supporting Information, Figure S15.

To support these data, radical trapping experiments were conducted using different scavengers to trap the active species while monitoring the reaction rate. The possible active species and their corresponding scavengers are summarized in Table S2. Ethanol (100 mM) and tert-butanol (100 mM) were added to trap hydroxyl and sulfate radicals, while sodium azide (100 mM) and p-benzoquinone (5 mM) were used to trap singlet oxygen and superoxide radical, respectively. Figure 7 shows that the addition of ethanol reduces the degradation rate substantially; however, when tert-butanol is added the degradation rate is reduced, albeit not reduced to the same degree as in the presence of ethanol. We believe that such a difference is ascribed to the disparity of rate constants for the reaction of hydroxyl radical with the tested scavengers. One possible explanation is that ethanol reacts with hydroxyl radicals ($k = 1.2-2.8 \times 10^9 \text{ M}^{-1} \text{ s}^{-1}$) much faster than tertbutanol $(k = 3.8 - 7.6 \times 10^8 \text{ M}^{-1} \text{ s}^{-1})$. This explains why the degradation rate was much slower when tert-butanol was replaced with ethanol. Other reports have attributed the difference in degradation rates to the presence of both sulfate and hydroxyl radicals; 64 however, the EPR data did not show any signal for the sulfate radicals, which might be attributed to the low concentration of sulfate radicals. The data also did not show any significant change on the degradation rate upon the addition of p-benzoquinone, which rules out the contribution of superoxide radicals in the degradation of atrazine. On the contrary, the suppression of the degradation rate upon the addition of sodium azide confirms the role of singlet oxygen as a nonradical ROS within the tested system. It is worth mentioning that p-benzoquinone reacts with superoxide radicals with a rate constant of $10^8 \sim 10^9$ L mol⁻¹ s^{-1.65} This finding was further validated by conducting the reaction under anaerobic conditions as displayed in Figure S16. The data reveal that the absence of oxygen has almost no effect on the rate of atrazine degradation, indicating that singlet oxygen is produced from PMS, rather than dissolved oxygen. Gao et al. 66 studied the generation of singlet oxygen in the metal-free peroxymonosulfate activation process and found that singlet oxygen was produced without any contribution of dissolved oxygen in reaction medium.

On the basis of these data, a PMS activation mechanism can be proposed as follows:

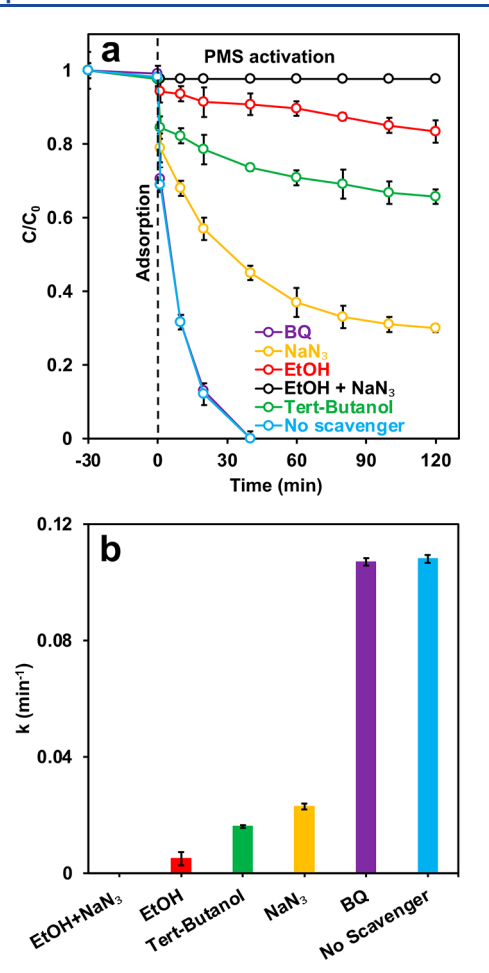


Figure 7. (a) Catalytic degradation and (b) pseudo-first-order rate constants of atrazine (4.6 µM) using Cu₂S@Bi₂S₃, 22 wt % (10 mg) and PMS (1 mM) in the presence of ethanol (100 mM), tert-butanol (100 mM), and NaN3 (100 mM) in a total volume of 50 mL.

$$Cu^{+} + HSO_{5}^{-} \rightarrow Cu^{2+} + SO_{4}^{2-} + OH^{\bullet}$$
 (1)

$$Cu^{2+} + HSO_5^- \rightarrow Cu^+ + SO_5^{\bullet -} + H^+$$
 (2)

$$Bi^{3+} + 2HSO_5^- \rightarrow Bi^{5+} + 2SO_4^{2-} + 2OH^{\bullet}$$
 (3)

$$Bi^{5+} + 2HSO_5^- \rightarrow Bi^{3+} + 2SO_5^{\bullet -} + 2H^+$$
 (4)

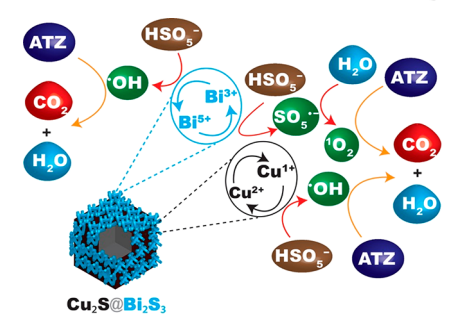
$$2SO_5^{\bullet -} + H_2O \rightarrow 1.5^1O_2 + 2HSO_4^{-}$$
 (5)

$$2S^{2-} + 2Cu^{2+} \rightarrow 2Cu^{+} + S_{2}^{2-}$$
 (6)

$$2S^{2-} + Bi^{5+} \to Bi^{3+} + S_2^{2-} \tag{7}$$

Accordingly, HSO₅⁻ is absorbed on the Cu₂S@Bi₂S₃ surface, which is then activated by Cu⁺ and Bi³⁺ to produce hydroxyl radicals and sulfate anions (eqs 1 and 3). The generated Cu2+ and Bi5+ activate some other HSO5 molecules to produce $SO_5^{\bullet -}$ (eqs 2 and 4), and thus, a redox cycle comprising the Cu^+/Cu^{2+} pair and Bi^{3+}/Bi^{5+} pair is established.^{67–70} Next, the generated $SO_5^{\bullet-}$ rapidly reacts with water molecules to produce singlet oxygen (eq 5).^{70,71} Moreover, the presence of S^{2-} can promote the recovery of S^{2-} and S^{3+} , which can enhance the PMS activation (eqs 6 and 7).⁷² Scheme 2 summarizes the proposed PMS activation mechanism over Cu₂S@Bi₂S₃. Thus, it can be concluded that the degradation of

Scheme 2. PMS Activation Mechanism over Cu₂S@Bi₂S₃



atrazine is totally driven by hydroxyl radicals and singlet oxygen as they are deemed the major active species within the system. Moreover, the synergy between Cu₂S and Bi₂S₃ promotes the radical generation and in turn enhances the catalytic performance.

To optimize the catalytic activity, different operating conditions were also investigated including catalyst amount, PMS concentration, reaction temperature, and pH. The effect of the amount of Cu₂S@Bi₂S₃ (22 wt %) used was investigated in the range 2.5-20 mg. Figure S17a,b reveals that the degradation extent is directly proportional to the catalyst amount; however, the 2.5 mg system was not able to completely degrade atrazine after 3 h. The enhancement of degradation rate upon increasing the Cu₂S@Bi₂S₃ amount can be ascribed to the abundance of active sites that act as a hub for the generation of reactive radicals.

The effect of PMS concentration was also investigated in the range 0.5-2 mM; the data reveal that the degradation rate (Figure S17c,d) increases with increasing PMS concentration owing to the generation of a higher number of active radicals. The time needed for complete degradation was shortened from 40 to 20 min after increasing the PMS concentration from 1 to 1.5 mM. Moreover, the increase in PMS concentration is not linear with the degradation rate, which can be ascribed to the competition between the additional PMS molecules and atrazine for the generated radicals.

The effect of operating temperature was also investigated in the range 10-40 °C, as shown in Figure S17e,f. The results reveal that the degradation rate increases with increasing the operating temperature, which can be attributed to minimizing the mass transfer limitations of the generated radicals. The obtained rate constants for different temperatures were used to calculate the activation energy (E_a) according to the following

$$\ln k = \ln A - \frac{E_{\rm a}}{RT} \tag{8}$$

where k is the rate constant, A is the pre-exponential factor, Ris the gas constant (8.31 JK mol^{-1}), and T is the temperature in Kelvin. The activation energy calculated from the slope of the Arrhenius plot displayed in Figure S18 was found to be 25.1 kJ mol⁻¹.

Next, the effect of pH was studied in the range 3-11 as presented in Figure S17g,h. It is evident that the degradation extent increases with increasing the system pH until pH = 9, and beyond this value, the degradation extent declines. The inferior performance under acidic conditions can be ascribed to the decomposition of PMS to produce $SO_4^{\ 2-.74}$ On the contrary, the decline in catalytic activity beyond pH = 9 can be ascribed to the deprotonation of PMS molecules under extremely drastic alkaline conditions to produce less reactive $SO_5^{-.75}$

To identify the intermediates produced during the degradation of atrazine within the tested system, HPLC–MS/MS analysis was conducted for aliquots collected during the course of the reaction. The molecular structure of the intermediates was identified according to the MS/MS fragmentation results with comparison to previously published data. We were able to identify a total of six intermediate products; the retention time, molecular weight, compound name, abbreviation, and structure of these products are listed in Table S3.

Previous studies reported that the presence of inorganic anions such as sulfate, nitrate, bicarbonate, and chloride ions in real wastewaters could substantially affect the degradation of organic contaminants. ^{78,79} To examine the effect of inorganic anions on atrazine degradation, different inorganic salts such as Na₂SO₄, NaNO₃, Na₂CO₃, Na₂HPO₄, and NaCl were added to the system while the degradation rate was monitored as displayed in Figure S19. It is evident that the suppression of the degradation rate upon the addition of inorganic anions can be arranged as $SO_4^{2-} > NO_3^- > H_2PO_4^- > HCO_3^- > Cl^-$ as displayed in Figure S19. Such suppression can be attributed to the reaction of the sulfate radicals and hydroxyl radicals with the inorganic anions to produce weak inorganic radicals. ^{80,81}

The stability of the prepared Cu₂S@Bi₂S₃ double-shelled cages was also evaluated for atrazine degradation in the presence of PMS by reusing the recovered catalyst for four cycles. After each cycle, the Cu₂S@Bi₂S₃ double-shelled cages were separated by centrifugation and dispersed again in a fresh atrazine solution. Figure S20 shows that the degradation of atrazine reached 100% after 40 min for the first run and 85% for the fourth. Furthermore, XRD analysis was conducted for the recovered Cu₂S@Bi₂S₃ catalyst after atrazine degradation, and the obtained pattern is presented in Figure S21. The data show a slight decrease in the crystallinity of the recovered catalyst, while the overall structure of Cu₂S@Bi₂S₃ was maintained. Moreover, SEM and TEM analyses were carried out after the reaction, and the obtained images are displayed in Figure S22. The images reveal that the morphology of the Cu₂S@Bi₂S₃ double-shelled cages remained unaltered. Thus, it is clear that the Cu₂S@Bi₂S₃ double-shelled cages are able to sustain the reaction conditions for multiple cycles.

To further study the versatility of the employed system to degrade different organic contaminants, catalytic activation of peroxymonosulfate (PMS) for the degradation of 4-nitrophenol (4-NP) and nitrobenzene (NB) was carried out. These organic compounds are commonly utilized in the manufacturing of herbicides, synthetic dyes, pesticides, and insecticides.⁸² Thus, large amounts of these compounds end up in the wastewater effluents of these industries, and the presence of such contaminants in the environment has a negative effect on the human health and the ecosystem.⁸³ These catalytic experiments were conducted using the same procedure employed for atrazine degradation, and the obtained data are presented in Figure S23 of the Supporting Information. The data revelated that complete degradation of 4-NP and NB using the employed system was obtained after 80 and 100 min, respectively. Thus, it can be concluded that the prepared Cu₂S@Bi₂S₃ double-shelled cages can be used as an effective catalyst to degrade a wide range of organic contaminants using the aforementioned conditions.

CONCLUSIONS

In conclusion, we demonstrated a multistage templating approach for the preparation of hierarchical double-shelled $\text{Cu}_2\text{S@Bi}_2\text{S}_3$ cages that hold unique structural and compositional properties. The preparation strategy can easily tailor the composition and structure of hierarchical double-layered materials that open up new horizons for a wide range of applications. Our data reveal that the catalytic performance of the studied materials increases in the order of $\text{Cu}_2\text{S@Bi}_2\text{S}_3$ (44 wt %) < Cu_2S < $\text{Cu}_2\text{S@Bi}_2\text{S}_3$ (22 wt %), where the complete degradation of atrazine was achieved in a relatively short time. The degradation of atrazine is driven exclusively by hydroxyl radicals and singlet oxygen as they are deemed the dominant active species within the tested system. Moreover, the synergy between Cu_2S and Bi_2S_3 nanoparticles promotes the radical generation and enhances the catalytic performance.

ASSOCIATED CONTENT

Supporting Information

The Supporting Information is available free of charge at https://pubs.acs.org/doi/10.1021/acsanm.1c02741.

Figures of EDS mapping and spectra, SEM and TEM images, NIR analysis, nitrogen adsorption-desorption isotherms, pore size distribution curves, adsorption of atrazine using different catalysts, catalytic degradation and pseudo-first-order rate constants of atrazine, X-band EPR spectra, optimization of atrazine degradation and pseudo-first-order rate constants, Arrhenius plot, effect of inorganic anions and pseudo-first-order rate constants, reusability of Cu₂S@Bi₂S₃, and XRD patterns, scheme of illustration of the preparation strategy of Cu₂S, tables of comparison of the rate constants, possible active species and their corresponding scavengers, and retention time, molecular weight, compound name, abbreviation and structure of atrazine and its degradation products, and discussion of analysis method of atrazine degradation products (PDF)

AUTHOR INFORMATION

Corresponding Author

Leonidas G. Bachas — Department of Chemistry, University of Miami, Coral Gables, Florida 33146, United States; Dr. J.T. Macdonald Foundation Biomedical Nanotechnology Institute, University of Miami, Miami, Florida 33136, United States; orcid.org/0000-0002-3308-6264; Email: bachas@miami.edu

Authors

Ahmed E. ElMetwally – Department of Chemistry, University of Miami, Coral Gables, Florida 33146, United States;
ocid.org/0000-0001-6746-6372

Farnoosh Goodarzi – DTU Chemistry, Technical University of Denmark, DK-2800 Kgs. Lyngby, Denmark

Katlyn K. Meier – Department of Chemistry, University of Miami, Coral Gables, Florida 33146, United States

Elsayed M. Zahran — Department of Chemistry, Ball State University, Muncie, Indiana 47306, United States; orcid.org/0000-0003-3456-515X

Sundeep Rayat — Department of Chemistry, Ball State University, Muncie, Indiana 47306, United States; orcid.org/0000-0002-0071-3110

Søren Kegnæs – DTU Chemistry, Technical University of Denmark, DK-2800 Kgs. Lyngby, Denmark; ⊙ orcid.org/ 0000-0002-6933-6931

Marc R. Knecht — Department of Chemistry, University of Miami, Coral Gables, Florida 33146, United States; Dr. J.T. Macdonald Foundation Biomedical Nanotechnology Institute, University of Miami, Miami, Florida 33136, United States; orcid.org/0000-0002-7614-7258

Complete contact information is available at: https://pubs.acs.org/10.1021/acsanm.1c02741

Author Contributions

All authors have given approval to the final version of the manuscript.

Notes

The authors declare no competing financial interest.

ACKNOWLEDGMENTS

Financial support by the University of Miami is gratefully acknowledged. Partial support is acknowledged from the National Science Foundation (M.R.K. - CHE 1903649). LC–MS spectra were obtained on an Ultimate 3000 Rapid Separation LC system coupled with a LTQ XL mass spectrometer (Thermo Fisher Scientific) supported by NSF-MRI grant under CHE-1531851.

REFERENCES

- (1) Li, H.; Shan, C.; Pan, B. Fe(III)-Doped g-C₃N₄ Mediated Peroxymonosulfate Activation for Selective Degradation of Phenolic Compounds via High-Valent Iron-Oxo Species. *Environ. Sci. Technol.* **2018**, 52 (4), 2197–2205.
- (2) Tang, L.; Liu, Y.; Wang, J.; Zeng, G.; Deng, Y.; Dong, H.; Feng, H.; Wang, J.; Peng, B. Enhanced activation process of persulfate by mesoporous carbon for degradation of aqueous organic pollutants: Electron transfer mechanism. *Appl. Catal., B* **2018**, *231*, 1–10.
- (3) Guo, S.; Wang, H.; Yang, W.; Fida, H.; You, L.; Zhou, K. Scalable synthesis of Ca-doped α -Fe₂O₃ with abundant oxygen vacancies for enhanced degradation of organic pollutants through peroxymonosulfate activation. *Appl. Catal., B* **2020**, *262*, 118250.
- (4) Guo, T.; Jiang, L.; Huang, H.; Li, Y.; Wu, X.; Zhang, G. Enhanced degradation of tetracycline in water over Cu-doped hematite nanoplates by peroxymonosulfate activation under visible light irradiation. *J. Hazard. Mater.* **2021**, *416*, 125838.
- (5) Guo, T.; Jiang, L.; Wang, K.; Li, Y.; Huang, H.; Wu, X.; Zhang, G. Efficient persulfate activation by hematite nanocrystals for degradation of organic pollutants under visible light irradiation: Facet-dependent catalytic performance and degradation mechanism. *Appl. Catal., B* **2021**, *286*, 119883.
- (6) Huang, H.; Guo, T.; Wang, K.; Li, Y.; Zhang, G. Efficient activation of persulfate by a magnetic recyclable rape straw biochar catalyst for the degradation of tetracycline hydrochloride in water. *Sci. Total Environ.* **2021**, 758, 143957.
- (7) Chen, Z.; He, S.; Zhu, M.; Wei, C. The effect of peroxymonosulfate in WS2 nanosheets for the removal of diclofenac: Information exposure and degradation pathway. *Chemosphere* **2020**, 245, 125678.
- (8) Yang, J.-C. E.; Zhu, M.-P.; Duan, X.; Wang, S.; Yuan, B.; Fu, M.-L. The mechanistic difference of 1T-2H MoS₂ homojunctions in persulfates activation: Structure-dependent oxidation pathways. *Appl. Catal., B* **2021**, *297*, 120460.
- (9) Ye, J.; Dai, J.; Yang, D.; Li, C.; Yan, Y.; Wang, Y. Interfacial engineering of vacancy-rich nitrogen-doped FexOy@MoS₂ Cocatalytic carbonaceous beads mediated non-radicals for fast catalytic oxidation. *J. Hazard. Mater.* **2022**, 421, 126715.
- (10) Zhang, J.; Peng, Z.; Soni, A.; Zhao, Y.; Xiong, Y.; Peng, B.; Wang, J.; Dresselhaus, M. S.; Xiong, Q. Raman Spectroscopy of Few-

- Quintuple Layer Topological Insulator Bi₂Se₃ Nanoplatelets. *Nano Lett.* **2011**, *11* (6), 2407–2414.
- (11) Zhou, X.; Cheng, J.; Zhou, Y.; Cao, T.; Hong, H.; Liao, Z.; Wu, S.; Peng, H.; Liu, K.; Yu, D. Strong Second-Harmonic Generation in Atomic Layered GaSe. *J. Am. Chem. Soc.* **2015**, *137* (25), 7994–7997.
- (12) Xie, J.; Zhang, J.; Li, S.; Grote, F.; Zhang, X.; Zhang, H.; Wang, R.; Lei, Y.; Pan, B.; Xie, Y. Controllable Disorder Engineering in Oxygen-Incorporated MoS₂ Ultrathin Nanosheets for Efficient Hydrogen Evolution. *J. Am. Chem. Soc.* **2013**, *135* (47), 17881–17888.
- (13) Li, Y.; Wang, H.; Xie, L.; Liang, Y.; Hong, G.; Dai, H. MoS₂ Nanoparticles Grown on Graphene: An Advanced Catalyst for the Hydrogen Evolution Reaction. *J. Am. Chem. Soc.* **2011**, *133* (19), 7296–7299.
- (14) Laursen, A. B.; Kegnæs, S.; Dahl, S.; Chorkendorff, I. Molybdenum sulfides—efficient and viable materials for electro-and photoelectrocatalytic hydrogen evolution. *Energy Environ. Sci.* **2012**, *5* (2), 5577–5591.
- (15) Zhao, W.; Zhang, C.; Geng, F.; Zhuo, S.; Zhang, B. Nanoporous Hollow Transition Metal Chalcogenide Nanosheets Synthesized via the Anion-Exchange Reaction of Metal Hydroxides with Chalcogenide Ions. *ACS Nano* **2014**, *8* (10), 10909–10919.
- (16) Zhou, W.; Wu, X.-J.; Cao, X.; Huang, X.; Tan, C.; Tian, J.; Liu, H.; Wang, J.; Zhang, H. Ni₃S₂ nanorods/Ni foam composite electrode with low overpotential for electrocatalytic oxygen evolution. *Energy Environ. Sci.* **2013**, 6 (10), 2921–2924.
- (17) Chen, X.; Yang, J.; Wu, T.; Li, L.; Luo, W.; Jiang, W.; Wang, L. Nanostructured binary copper chalcogenides: synthesis strategies and common applications. *Nanoscale* **2018**, *10* (32), 15130–15163.
- (18) Chakrabarti, D. J.; Laughlin, D. E. The Cu-S (Copper-Sulfur) system. Bull. Alloy Phase Diagrams 1983, 4 (3), 254.
- (19) Martinson, A. B. F.; Elam, J. W.; Pellin, M. J. Atomic layer deposition of Cu₂S for future application in photovoltaics. *Appl. Phys. Lett.* **2009**, *94* (12), 123107.
- (20) Chen, Y.-B.; Chen, L.; Wu, L.-M. The Structure-Controlling Solventless Synthesis and Optical Properties of Uniform Cu₂S Nanodisks. *Chem. Eur. J.* **2008**, *14* (35), 11069–11075.
- (21) An, L.; Zhou, P.; Yin, J.; Liu, H.; Chen, F.; Liu, H.; Du, Y.; Xi, P. Phase Transformation Fabrication of a Cu_2S Nanoplate as an Efficient Catalyst for Water Oxidation with Glycine. *Inorg. Chem.* **2015**, *54* (7), 3281–3289.
- (22) Li, Z.; Chen, W.; Ji, S.; Mi, L.; Hou, H.; Zheng, Z. Structural and catalytic properties of Cu₂S microrods grown on a three-dimensional substrate. *Cryst. Res. Technol.* **2012**, 47 (1), 87–90.
- (23) Liu, Y.; Deng, Y.; Sun, Z.; Wei, J.; Zheng, G.; Asiri, A. M.; Khan, S. B.; Rahman, M. M.; Zhao, D. Hierarchical Cu₂S Microsponges Constructed from Nanosheets for Efficient Photocatalysis. *Small* **2013**, *9* (16), 2702–2708.
- (24) Wang, H.; Jiang, L.; Chen, T.; Li, Y. A Highly Efficient, Ligand-Free, and Recyclable Cu2S-Catalyzed Coupling of Aryl Iodides with Diaryl Disulfides. *Eur. J. Org. Chem.* **2010**, 2010 (12), 2324–2329.
- (25) Park, K.-H.; Lee, Y. W.; Kim, D.; Lee, K.; Lee, S. B.; Han, S. W. Synthesis and Photocatalytic Properties of Cu₂S-Pd₄S Hybrid Nanoplates. *Chem. Eur. J.* **2012**, *18* (19), 5874–5878.
- (26) Zhang, X.; Guo, Y.; Tian, J.; Sun, B.; Liang, Z.; Xu, X.; Cui, H. Controllable growth of MoS₂ nanosheets on novel Cu₂S snowflakes with high photocatalytic activity. *Appl. Catal., B* **2018**, 232, 355–364.
- (27) Wang, H.; Liu, L.; Wang, Y.; Lin, S.; An, W.; Cui, W.; Liang, Y. Cu₂S nanoparticles modified 3D flowerlike Bi₂WO₆: Enhanced photoelectric performance and photocatalytic degradation. *Mater. Lett.* **2015**, *160*, 351–354.
- (28) Fakhravar, S.; Farhadian, M.; Tangestaninejad, S. Excellent performance of a novel dual Z-scheme $Cu_2S/Ag_2S/BiVO_4$ heterostructure in metronidazole degradation in batch and continuous systems: Immobilization of catalytic particles on α -Al $_2O_3$ fiber. *Appl. Surf. Sci.* **2020**, *505*, 144599.
- (29) Rabin, O.; Manuel Perez, J.; Grimm, J.; Wojtkiewicz, G.; Weissleder, R. An X-ray computed tomography imaging agent based

- on long-circulating bismuth sulphide nanoparticles. *Nat. Mater.* **2006**, 5 (2), 118–122.
- (30) Bao, H.; Li, C. M.; Cui, X.; Gan, Y.; Song, Q.; Guo, J. Synthesis of a Highly Ordered Single-Crystalline $\mathrm{Bi}_2\mathrm{S}_3$ Nanowire Array and its Metal/Semiconductor/Metal Back-to-Back Schottky Diode. *Small* **2008**, *4* (8), 1125–1129.
- (31) Ma, J.; Liu, Z.; Lian, J.; Duan, X.; Kim, T.; Peng, P.; Liu, X.; Chen, Q.; Yao, G.; Zheng, W. Ionic liquids-assisted synthesis and electrochemical properties of Bi₂S₃ nanostructures. *CrystEngComm* **2011**, *13* (8), 3072–3079.
- (32) Yao, K.; Gong, W. W.; Hu, Y. F.; Liang, X. L.; Chen, Q.; Peng, L. M. Individual Bi2S3 Nanowire-Based Room-Temperature H₂ Sensor. *J. Phys. Chem. C* **2008**, *112* (23), 8721–8724.
- (33) Luo, Y.; Chen, H.; Li, X.; Gong, Z.; Wang, X.; Peng, X.; He, M.; Sheng, Z. Wet chemical synthesis of Bi₂S₃ nanorods for efficient photocatalysis. *Mater. Lett.* **2013**, *105*, 12–15.
- (34) Huang, Y.; Fan, W.; Long, B.; Li, H.; Zhao, F.; Liu, Z.; Tong, Y.; Ji, H. Visible light Bi₂S₃/Bi₂O₃/Bi₂O₂CO₃ photocatalyst for effective degradation of organic pollutions. *Appl. Catal., B* **2016**, *185*, 68–76
- (35) Cui, Y.; Jia, Q.; Li, H.; Han, J.; Zhu, L.; Li, S.; Zou, Y.; Yang, J. Photocatalytic activities of Bi₂S₃/BiOBr nanocomposites synthesized by a facile hydrothermal process. *Appl. Surf. Sci.* **2014**, *290*, 233–239.
- (36) Zhang, Z.; Wang, W.; Wang, L.; Sun, S. Enhancement of Visible-Light Photocatalysis by Coupling with Narrow-Band-Gap Semiconductor: A Case Study on Bi₂S₃/Bi₂WO₆. ACS Appl. Mater. Interfaces **2012**, 4 (2), 593–597.
- (37) Cao, J.; Xu, B.; Lin, H.; Luo, B.; Chen, S. Novel Bi₂S₃-sensitized BiOCl with highly visible light photocatalytic activity for the removal of rhodamine B. *Catal. Commun.* **2012**, *26*, 204–208.
- (38) Imam, S. S.; Adnan, R.; Mohd Kaus, N. H. Room-temperature synthesis of flower-like BiOBr/Bi₂S₃ composites for the catalytic degradation of fluoroquinolones using indoor fluorescent light illumination. *Colloids Surf., A* **2020**, *585*, 124069.
- (39) Chen, X.; Li, Q.; Li, J.; Chen, J.; Jia, H. Modulating charge separation via in situ hydrothermal assembly of low content Bi₂S₃ into UiO-66 for efficient photothermocatalytic CO₂ reduction. *Appl. Catal., B* **2020**, 270, 118915.
- (40) Huang, K.; Sun, Y.; Zhang, Y.; Wang, X.; Zhang, W.; Feng, S. Hollow-Structured Metal Oxides as Oxygen-Related Catalysts. *Adv. Mater.* **2019**, *31* (38), 1801430.
- (41) Prieto, G.; Tüysüz, H.; Duyckaerts, N.; Knossalla, J.; Wang, G.-H.; Schüth, F. Hollow Nano- and Microstructures as Catalysts. *Chem. Rev.* **2016**, *116* (22), 14056–14119.
- (42) Zhou, L.; Shao, M.; Wei, M.; Duan, X. Advances in efficient electrocatalysts based on layered double hydroxides and their derivatives. *J. Energy Chem.* **2017**, *26* (6), 1094–1106.
- (43) Yu, L.; Hu, H.; Wu, H. B.; Lou, X. W. Complex Hollow Nanostructures: Synthesis and Energy-Related Applications. *Adv. Mater.* **2017**, 29 (15), 1604563.
- (44) Miller, E. B.; Zahran, E. M.; Knecht, M. R.; Bachas, L. G. Metal oxide semiconductor nanomaterial for reductive debromination: Visible light degradation of polybrominated diphenyl ethers by Cu₂O@Pd nanostructures. *Appl. Catal., B* **2017**, *213*, 147–154.
- (45) Zahran, E. M.; Bedford, N. M.; Nguyen, M. A.; Chang, Y.-J.; Guiton, B. S.; Naik, R. R.; Bachas, L. G.; Knecht, M. R. Light-Activated Tandem Catalysis Driven by Multicomponent Nanomaterials. J. Am. Chem. Soc. 2014, 136 (1), 32–35.
- (46) ElMetwally, A. E.; Zeynaloo, E.; Shukla, D.; Surnar, B.; Dhar, S.; Cohn, J. L.; Knecht, M. R.; Bachas, L. G. Cu₂O Cubes Decorated with Azine-Based Covalent Organic Framework Spheres and Pd Nanoparticles as Tandem Photocatalyst for Light-Driven Degradation of Chlorinated Biphenyls. ACS Appl. Nano Mater. 2021, 4 (3), 2795–2805.
- (47) Petasis, D. T.; Hendrich, M. P. Quantitative Interpretation of Multifrequency Multimode EPR Spectra of Metal Containing Proteins, Enzymes, and Biomimetic Complexes. *Methods Enzymol.* **2015**, *563*, 171–208.

- (48) Jiao, S.; Xu, L.; Jiang, K.; Xu, D. Well-Defined Non-spherical Copper Sulfide Mesocages with Single-Crystalline Shells by Shape-Controlled Cu₂O Crystal Templating. *Adv. Mater.* **2006**, *18* (9), 1174–1177
- (49) Jiang, Z.; Yang, F.; Yang, G.; Kong, L.; Jones, M. O.; Xiao, T.; Edwards, P. P. The hydrothermal synthesis of BiOBr flakes for visible-light-responsive photocatalytic degradation of methyl orange. *J. Photochem. Photobiol., A* **2010**, 212 (1), 8–13.
- (50) Li, T.; Wu, H.; Li, H.; Chen, S.; Zhang, D.; Xu, F. Aminoterminated hyperbranched polyamide regulating Cu₂S twin-daffodil with enhanced sodium-storage performance. *Mater. Chem. Phys.* **2020**, 248, 122934.
- (51) He, H.; Berglund, S. P.; Xiao, P.; Chemelewski, W. D.; Zhang, Y.; Mullins, C. B. Nanostructured Bi₂S₃/WO₃ heterojunction films exhibiting enhanced photoelectrochemical performance. *J. Mater. Chem. A* **2013**, *1* (41), 12826–12834.
- (52) Ye, M.; Chen, C.; Zhang, N.; Wen, X.; Guo, W.; Lin, C. Quantum-Dot Sensitized Solar Cells Employing Hierarchical Cu₂S Microspheres Wrapped by Reduced Graphene Oxide Nanosheets as Effective Counter Electrodes. *Adv. Energy Mater.* **2014**, *4* (9), 1301564.
- (53) Kuo, C.-H.; Chu, Y.-T.; Song, Y.-F.; Huang, M. H. Cu_2O Nanocrystal-Templated Growth of Cu_2S Nanocages with Encapsulated Au Nanoparticles and In-Situ Transmission X-ray Microscopy Study. *Adv. Funct. Mater.* **2011**, 21 (4), 792–797.
- (54) Wang, Y.; Tian, W.; Chen, L.; Cao, F.; Guo, J.; Li, L. Three-Dimensional WO₃ Nanoplate/Bi₂S₃ Nanorod Heterojunction as a Highly Efficient Photoanode for Improved Photoelectrochemical Water Splitting. ACS Appl. Mater. Interfaces **2017**, 9 (46), 40235–40243.
- (55) Bell, E. C.; Munro, C. J.; Slocik, J. M.; Shukla, D.; Parab, A. D.; Cohn, J. L.; Knecht, M. R. Biomimetic strategies to produce catalytically reactive CuS nanodisks. *Nanoscale Adv.* **2019**, *1* (8), 2857–2865.
- (56) Liu, Y.; Liu, M.; Swihart, M. T. Plasmonic Copper Sulfide-Based Materials: A Brief Introduction to Their Synthesis, Doping, Alloying, and Applications. *J. Phys. Chem. C* **2017**, *121* (25), 13435–13447.
- (57) Li, J.; Wan, Y.; Li, Y.; Yao, G.; Lai, B. Surface Fe(III)/Fe(II) cycle promoted the degradation of atrazine by peroxymonosulfate activation in the presence of hydroxylamine. *Appl. Catal., B* **2019**, 256, 117782.
- (58) Chan, K. H.; Chu, W. Degradation of atrazine by cobalt-mediated activation of peroxymonosulfate: Different cobalt counteranions in homogenous process and cobalt oxide catalysts in photolytic heterogeneous process. *Water Res.* **2009**, *43* (9), 2513–2521.
- (59) Wang, G.; Cheng, C.; Zhu, J.; Wang, L.; Gao, S.; Xia, X. Enhanced degradation of atrazine by nanoscale LaFe_{1-x}Cu_xO_{3- δ} perovskite activated peroxymonosulfate: Performance and mechanism. *Sci. Total Environ.* **2019**, *673*, 565–575.
- (60) Zhang, R.; Wan, Y.; Peng, J.; Yao, G.; Zhang, Y.; Lai, B. Efficient degradation of atrazine by LaCoO₃/Al₂O₃ catalyzed peroxymonosulfate: Performance, degradation intermediates and mechanism. *Chem. Eng. J.* **2019**, *372*, 796–808.
- (61) Zhou, X.; Luo, M.; Xie, C.; Wang, H.; Wang, J.; Chen, Z.; Xiao, J.; Chen, Z. Tunable S doping from Co₃O₄ to Co₉S₈ for peroxymonosulfate activation: Distinguished Radical/Nonradical species and generation pathways. *Appl. Catal., B* **2021**, 282, 119605.
- (62) Fang, G.-D.; Zhou, D.-M.; Dionysiou, D. D. Superoxide mediated production of hydroxyl radicals by magnetite nanoparticles: Demonstration in the degradation of 2-chlorobiphenyl. *J. Hazard. Mater.* **2013**, 250–251, 68–75.
- (63) Liang, C.; Su, H.-W. Identification of Sulfate and Hydroxyl Radicals in Thermally Activated Persulfate. *Ind. Eng. Chem. Res.* **2009**, 48 (11), 5558–5562.
- (64) Tan, C.; Gao, N.; Deng, Y.; Deng, J.; Zhou, S.; Li, J.; Xin, X. Radical induced degradation of acetaminophen with Fe₃O₄ magnetic nanoparticles as heterogeneous activator of peroxymonosulfate. *J. Hazard. Mater.* **2014**, 276, 452–460.

- (65) Zhu, M.; Lu, J.; Hu, Y.; Liu, Y.; Hu, S.; Zhu, C. Photochemical reactions between 1,4-benzoquinone and $O_2^{\bullet^-}$. *Environ. Sci. Pollut. Res.* **2020**, 27 (25), 31289–31299.
- (66) Gao, Y.; Chen, Z.; Zhu, Y.; Li, T.; Hu, C. New Insights into the Generation of Singlet Oxygen in the Metal-Free Peroxymonosulfate Activation Process: Important Role of Electron-Deficient Carbon Atoms. *Environ. Sci. Technol.* **2020**, *54* (2), 1232–1241.
- (67) Ding, Y.; Zhu, L.; Wang, N.; Tang, H. Sulfate radicals induced degradation of tetrabromobisphenol A with nanoscaled magnetic CuFe₂O₄ as a heterogeneous catalyst of peroxymonosulfate. *Appl. Catal.*. B **2013**. *129*. 153–162.
- (68) Li, J.; Ye, P.; Fang, J.; Wang, M.; Wu, D.; Xu, A.; Li, X. Peroxymonosulfate activation and pollutants degradation over highly dispersed CuO in manganese oxide octahedral molecular sieve. *Appl. Surf. Sci.* **2017**, 422, 754–762.
- (69) Tang, W.; Zhang, Y.; Guo, H.; Liu, Y. Heterogeneous activation of peroxymonosulfate for bisphenol AF degradation with BiO_{10.5}Cl_{0.5}. RSC Adv. **2019**, 9 (25), 14060–14071.
- (70) Liu, Y.; Guo, H.; Zhang, Y.; Tang, W.; Cheng, X.; Li, W. Heterogeneous activation of peroxymonosulfate by sillenite Bi₂₅FeO₄₀: Singlet oxygen generation and degradation for aquatic levofloxacin. *Chem. Eng. J.* **2018**, 343, 128–137.
- (71) Wang, S.; Tian, J.; Wang, Q.; Xiao, F.; Gao, S.; Shi, W.; Cui, F. Development of CuO coated ceramic hollow fiber membrane for peroxymonosulfate activation: a highly efficient singlet oxygendominated oxidation process for bisphenol a degradation. *Appl. Catal., B* **2019**, *256*, 117783.
- (72) Wang, S.; Wang, J. Peroxymonosulfate activation by $Co_9S_8@S$ and N co-doped biochar for sulfamethoxazole degradation. *Chem. Eng. J.* **2020**, 385, 123933.
- (73) Guo, Y.; Lou, X.; Fang, C.; Xiao, D.; Wang, Z.; Liu, J. Novel Photo-Sulfite System: Toward Simultaneous Transformations of Inorganic and Organic Pollutants. *Environ. Sci. Technol.* **2013**, 47 (19), 11174–11181.
- (74) Chen, T.; Zhu, Z.; Wang, Z.; Zhang, H.; Qiu, Y.; Yin, D.; Zhao, G. 3D hollow sphere-like Cu-incorporated LaAlO₃ perovskites for peroxymonosulfate activation: Coaction of electron transfer and oxygen defect. *Chem. Eng. J.* **2020**, 385, 123935.
- (75) Ma, Q.; Zhang, H.; Zhang, X.; Li, B.; Guo, R.; Cheng, Q.; Cheng, X. Synthesis of magnetic CuO/MnFe₂O₄ nanocompisite and its high activity for degradation of levofloxacin by activation of persulfate. *Chem. Eng. J.* **2019**, *360*, 848–860.
- (76) Wu, S.; Li, H.; Li, X.; He, H.; Yang, C. Performances and mechanisms of efficient degradation of atrazine using peroxymonosulfate and ferrate as oxidants. *Chem. Eng. J.* **2018**, 353, 533–541.
- (77) Huang, Y.; Han, C.; Liu, Y.; Nadagouda, M. N.; Machala, L.; O'Shea, K. E.; Sharma, V. K.; Dionysiou, D. D. Degradation of atrazine by $Zn_xCu_{1-x}Fe_2O_4$ nanomaterial-catalyzed sulfite under UV-vis light irradiation: Green strategy to generate SO_4^- . *Appl. Catal., B* **2018**, 221, 380–392.
- (78) Sun, Z.; Liu, X.; Dong, X.; Zhang, X.; Tan, Y.; Yuan, F.; Zheng, S.; Li, C. Synergistic activation of peroxymonosulfate via in situ growth $FeCo_2O_4$ nanoparticles on natural rectorite: Role of transition metal ions and hydroxyl groups. *Chemosphere* **2021**, 263, 127965.
- (79) Hu, L.; Zhang, G.; Liu, M.; Wang, Q.; Wang, P. Enhanced degradation of Bisphenol A (BPA) by peroxymonosulfate with Co₃O₄-Bi₂O₃ catalyst activation: Effects of pH, inorganic anions, and water matrix. *Chem. Eng. J.* **2018**, 338, 300–310.
- (80) Liu, B.; Guo, W.; Wang, H.; Zheng, S.; Si, Q.; Zhao, Q.; Luo, H.; Ren, N. Peroxymonosulfate activation by cobalt(II) for degradation of organic contaminants via high-valent cobalt-oxo and radical species. *J. Hazard. Mater.* **2021**, *416*, 125679.
- (81) Li, C.; Huang, Y.; Dong, X.; Sun, Z.; Duan, X.; Ren, B.; Zheng, S.; Dionysiou, D. D. Highly efficient activation of peroxymonosulfate by natural negatively-charged kaolinite with abundant hydroxyl groups for the degradation of atrazine. *Appl. Catal., B* **2019**, 247, 10–23.
- (82) Dieckmann, M. S.; Gray, K. A. A comparison of the degradation of 4-nitrophenol via direct and sensitized photocatalysis in TiO₂ slurries. *Water Res.* **1996**, *30* (5), 1169–1183.

(83) Takahashi, N.; Nakai, T.; Satoh, Y.; Katoh, Y. Variation of biodegradability of nitrogenous organic compounds by ozonation. *Water Res.* **1994**, 28 (7), 1563–1570.